

ALMA OBSERVATIONS OF HCO⁺ AND HCN EMISSION IN A MASSIVE STAR FORMING REGION N 55 OF THE LARGE MAGELLANIC CLOUD

NAYANA A.J.,¹ NASLIM N.,^{1,2,3} T. ONISHI,⁴ F. KEMPER,^{5,2} K. TOKUDA,⁴ S. C. MADDEN,⁶ O. MORATA,⁵ S. NASRI,¹ AND M. GALAMETZ⁶

¹*Department of physics, United Arab Emirates University, Al-Ain, UAE, 15551.*

²*Academia Sinica Institute of Astronomy and Astrophysics, Taipei 10617, Taiwan R.O.C*

³*Armagh Observatory, College Hill, Armagh, Northern Ireland, UK, BT61 9DG*

⁴*Department of Physical Science, Graduate School of Science, Osaka Prefecture University, 1-1 Gakuen-cho, Sakai, Osaka 599-8531, Japan*

⁵*European Southern Observatory, Karl-Schwarzschild-Str. 2, 85748, Garching b. Mnchen, Germany*

⁶*Laboratoire AIM, CEA/DSM - CEA Saclay, 91191 Gif-sur-Yvette, France*

Submitted to ApJ

ABSTRACT

We present the results of high spatial resolution HCO⁺(1 – 0) and HCN(1 – 0) observations of N 55 south region (N 55-S) in the Large Magellanic Cloud (LMC), obtained with the Atacama Large Millimeter/submillimeter Array (ALMA). N 55-S is a relatively less extreme star-forming region of the LMC characterized by a low radiation field. We carried out a detailed analysis of the molecular emission to investigate the relation between dense molecular clumps and star formation in the quiescent environment of N 55-S. We detect ten molecular clumps with significant HCO⁺(1 – 0) emission and eight with significant HCN(1 – 0) emission, and estimate the molecular clump masses by virial and local thermodynamic equilibrium analysis. All identified young stellar objects (YSOs) in the N 55-S are found to be near the HCO⁺ and HCN emission peaks showing the association of these clumps with recent star formation activity. The molecular clumps that have associated YSOs show relatively larger linewidths and masses than those without YSOs. We compare the clump properties of the N 55-S with those of other giant molecular clouds (GMCs) in the LMC and find that N 55-S clumps possess similar size but relatively lower linewidth and larger HCN/HCO⁺(1–0) flux ratio. These results can be attributed to the low radiation field in N 55-S resulted by relatively low star formation activity compared to other active star-forming regions like 30 Doradus-10 and N 159. The dense gas fraction of N 55-S is ~ 0.025 , lower compared to other GMCs of the LMC supporting the low star formation efficiency of this region.

Keywords: galaxies: individual (LMC) — stars: formation

1. INTRODUCTION

Massive stars form as clusters in the densest clumps of Giant Molecular Clouds (GMCs). These clumps are self-gravitating parsec sized structures that collapse and fragment into dense cores to form high-mass stars (Williams et al. 2000). The physical processes that determine the fragmentation of GMCs to clumps and cores depend on the star formation history, cooling due to the build-up of metals and feedback from massive stars. Different star-forming environments can change the properties of GMCs and its sub-structure. Thus it is important to look at the GMCs and their sub-structure in different feedback environments to study star formation in galaxies.

Star formation studies on galaxy wide scale exist for the Milky Way (Kennicutt & Evans 2012). However, studying star formation in other galaxies is limited due to the lack of high-resolution instruments that can resolve the dense molecular clumps of GMCs. Such studies can be done in the Large Magellanic Cloud (LMC) due to its proximity. At a distance of 49.59 kpc (Pietrzyński et al. 2019), high spatial resolution observations of molecular clouds at sub-parsec scale can be obtained. Several massive star forming GMCs of the LMC has been studied extensively. These include 30-Doradus (Nayak et al. 2016; Indebetouw et al. 2020), N159 (Nayak et al. 2018; Fukui et al. 2015; Chen et al. 2010), N44 (Chen et al. 2009, 2010), N113 (Wong et al. 2006; Carlson et al. 2012) and N105 (Ambrocio-Cruz et al. 1998; Carlson et al. 2012). The presence of stellar cluster R136 and numerous OB stars makes 30-Doradus the most extreme star forming GMC of the LMC (Nayak et al. 2016; Hughes et al. 2010; Pineda et al. 2009). N159 is also a region of intense radiation field $\sim 156\chi_0$ ($\chi_0 = 2.7 \times 10^{-3} \text{ erg s}^{-1} \text{ cm}^{-2}$; Draine 1978), high turbulence and shocks (Nayak et al. 2018; Fukui et al. 2015). With only 11 identified OB stars (Olsen et al. 2001) and a radiation field of $18\chi_0$ (Pineda et al. 2009), N55 is an example of quiescent star forming environment of the LMC.

N55 is a star forming region of size $\sim 60 \times 100 \text{ pc}^2$ located in the super-giant shell LMC4 (see Fig 1; Yamaguchi et al. 2001). While the bulk of LMC4 is empty of ionized gas, N55 stands out as a bright HII region in the H α map (Olsen et al. 2001). The *Spitzer* observations of N55 show filamentary distribution of Polycyclic Aromatic Hydrocarbon (PAH; Fig 1; Naslim et al. 2018). A total of 16 YSOs has been identified in the N55 from *Spitzer* photometric observations indicating on-going star formation (Gruendl, & Chu 2009; Seale et al. 2014). Naslim et al. (2015) detected the H₂ rotational transitions at 28.2 and 17.1 μm in the

N55 main molecular cloud complex with the infrared spectrograph onboard *Spitzer* space telescope. Their studies shows a tight correlation of H₂ surface brightness with the PAH and total infrared emission indicating photoelectric heating caused by UV radiation from massive stars. The ¹²CO(1–0) and ¹³CO(1–0) observations of N55 reveals the clumpy nature of molecular gas with a total mass of $\sim 5.4 \times 10^4 \text{ M}_\odot$ (Naslim et al. 2018).

CO isotopes probe molecular gas from relatively low-density regions ($\sim 10^2 \text{ cm}^{-3}$) whereas HCO⁺(1–0) and HCN(1–0) trace dense molecular clumps due to their high critical densities ($\sim 10^{4-5} \text{ cm}^{-3}$). In this paper, we present the HCO⁺(1–0) and HCN(1–0) observations of the main molecular complex towards the south of the N55 (here onwards N55-S; see Fig 1) with the Atacama Large Millimeter/submillimeter Array (ALMA). This is first time HCO⁺ and HCN emission are observed toward N55. Our study aims to investigate the physical properties such as size, linewidth, mass, and dense gas fraction of the dense molecular clumps in a relatively quiescent region in the LMC. Seale et al. (2012) studied molecular clumps of different star-forming GMCs of the LMC (N159, N105A, N44, and N113) using the same dense gas tracers. A similar study was carried out by Anderson et al. (2014) in the 30 Doradus-10. Our work extends this sample including N55-S with a goal to explore how different star formation environments affect the properties of dense molecular clumps. We compare the physical properties and scaling relation of the dense molecular clumps of the N55-S with other extreme star-forming environments, mainly 30-Doradus (Anderson et al. 2014) and N159 (Seale et al. 2012).

The paper is organized as follows. We describe the ALMA observations and data analysis in §2 and present the regions of molecular emission in §3. The clump identification and physical properties of each clump are presented in §4. In §5, we inspect the spatial extent of dense gas tracers and CO isotopes to understand the density structure of the molecular cloud. We discuss the spatial coincidence of young stellar objects (YSOs) with the dense gas tracers and interpret the results in light of ongoing star formation in §6. Finally, We compare the properties of the molecular clumps of the N55 cloud with other GMCs of the LMC in §7. We summarize our results in §8.

2. ALMA OBSERVATIONS

The ALMA observations of N55 main molecular complex were carried out in cycle 3 (project code 2013.1.00993.S) on 19 January 2015. The observations were done with the ALMA 12 m array in the band 3 in two frequency settings covering the HCN(1 – 0)

and HCO⁺(1–0) lines at rest frequencies 88.6318 and 89.1885 GHz, respectively. The field of view of the observation is $\sim 3.5 \times 2$ arcmin², centered at RA, Dec (J2000): 05:32:31.50; –66:26:22.5 covering $\sim 50 \times 29$ pc² in linear scale. Our observation is towards the southern region of N 55 (N 55-S) that covers the main molecular complex of N 55 and does not cover the entire N 55. The observations were carried out for a total integration time of 796 seconds. The correlator was set to have a bandwidth of 117.187 MHz split into 1920 channels in each spectral window. This corresponds to a native spectral resolution of 61 kHz (0.2 km s^{–1}). We binned the channels to a resolution of 0.4 km s^{–1} for the analysis.

The data were reduced using common astronomy software application (CASA; McMullin et al. 2007) package. Uranus was used as the flux calibrator and J0526–6749 was used as the phase calibrator. The ALMA pipeline calibrated visibilities were imaged using CASA task TCLEAN with a channel resolution of 0.4 km s^{–1}. We applied the Briggs weighting with a robust parameter of 0.5. The achieved rms sensitivities per 0.4 km s^{–1} channel for HCO⁺(1–0) and HCN(1–0) cubes are ~ 10 and 11 mJy beam^{–1} respectively. The synthesized beam of HCO⁺(1–0) map is $4.07'' \times 3.11''$ which translates to a linear size of 0.98×0.74 pc² at the LMC distance. For HCN(1–0) map, the synthesized beam is $4.13'' \times 3.14''$ which corresponds to 0.99×0.75 pc² in linear scale.

3. HCO AND HCN EMISSION IN N 55

The velocity integrated intensity maps of HCO⁺(1–0) and HCN(1–0) emission are shown in Fig 2. These maps are obtained by integrating the emission line data cubes along the velocity axis. The maps show the clumpy nature of dense molecular gas in N 55-S at parsec scales. The emission structures are mostly discrete, rather than nested or filamentary. A visual inspection suggests that the HCO⁺(1–0) emission from each molecular clump originates from slightly extended regions as compared to HCN(1–0). This could be due to the higher densities probed by HCN(1–0) emission as compared to HCO⁺(1–0). A similar trend in the spatial distribution of HCO⁺(1–0) and HCN(1–0) emission in molecular clumps has been reported in N 105, N 113, N 159 and N 44 regions (Seale et al. 2012). The positions of YSOs in the N 55-S region identified by *Spitzer* observations (Gruendl, & Chu 2009; Chen et al. 2009) are shown along with HCO⁺(1–0) and HCN(1–0) clumps in Fig 2. The YSO positions are near the emission peaks of the clumps. The ¹²CO(1–0) and ¹³CO(1–0) maps

of N 55-S (Naslim et al. 2018) is also shown for a comparison which is discussed in §5.

4. CLUMP IDENTIFICATION AND CHARACTERIZATION

We use **astrodendro**¹ (a python package) to identify emission structures from the data cube. The algorithm identifies the hierarchical structure of emission (Rosolowsky et al. 2008). Local maxima are identified from the data cube each with flux $> 3\sigma_{\text{rms}}$ and the iso-surfaces around the maxima are classified as leaves, branches or trunks. If the iso-surfaces do not have any sub-structures, they are categorized as leaves. The largest contiguous structures in the cube are identified as trunks. The structures intermediate to leaves and trunks are classified as branches. Thus in a dendrogram, leaves do not overlap each other and they are the smallest emission clumps without sub-structures.

Astrodendro determines the basic parameters of the identified structures using the bisection method. The parameters are the velocity and positional centroids, integrated flux density, velocity dispersion (ie. rms linewidth σ_v), rms sizes of the major (σ_{maj}) and minor (σ_{min}) axes of the clump and the position angle of the major axis. For Gaussian line profiles, the FWHM linewidth (Δv) is given by $\Delta v = \sqrt{8 \ln(2)} \sigma_v$. The spherical radius of the clump is $R = 1.91\sigma_r$ where $\sigma_r = \sqrt{\sigma_{\text{maj}}\sigma_{\text{min}}}$. We use bootstrapping technique to determine the uncertainties in the derived parameters.

We identify 10 significant molecular clumps in the HCO⁺(1–0) and 8 in the HCN(1–0) data cubes. These are all identified as leaves by **astrodendro**. The properties of all these structures are listed in Table 1. For the resolution of our observations, we can resolve only clumps of size ≥ 4 arcsec. This translates to ~ 1 pc at the LMC distance. The sizes of identified clumps are 1 – 2.2 pc, except for one clump (clump id = 6) with size 0.82 pc. The sizes of dense molecular clumps in the massive star-forming regions of the Milky Way Galaxy is $\sim 0.1 - 1$ pc (Retes-Romero et al. 2017). Given the limit in our spatial resolution, the smallest detected molecular structures in the N 55-S seem compatible with the Milky Way clumps.

We present HCO⁺(1–0) emission spectra of all ten identified clumps of the N 55-S in Fig 3. We assert that all detections are strong with HCO⁺(1–0) emission peaks detected with a minimum spectral signal to noise ratio of 4. We note an additional red-shifted feature in the spectrum of clump 9, possibly due to any dynamical activity in this region. The HCN/HCO⁺ flux

¹ <http://www.dendrograms.org>

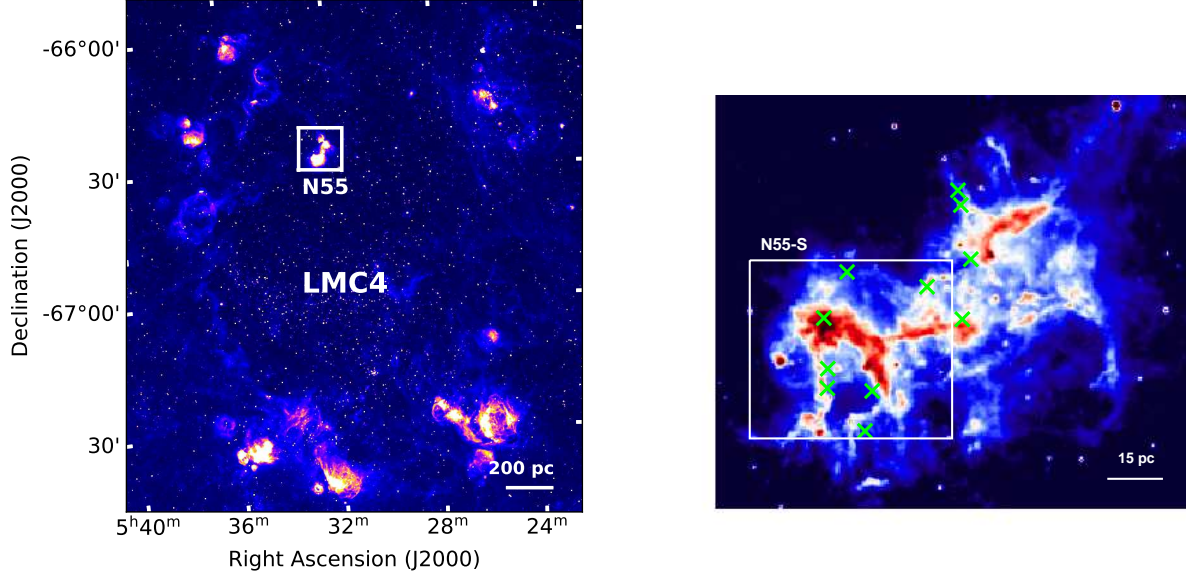


Figure 1. Left panel: The super-giant shell LMC 4 is shown on an $H\alpha$ image (Smith & MCELS Team 1998). The location of N 55 star forming region is marked. Right panel: The structure of N 55 is shown in *Spitzer* $8.0\mu\text{m}$ image (Meixner et al. 2010) which traces the filamentary PAH emission. The white box indicates the location of N 55-S. The 11 OB stars are labelled in crosses (Olsen et al. 2001).

ratio of the clumps ranges from 0.46 ± 0.17 to 0.78 ± 0.12 (see Table 1), indicating overall weaker HCN flux in N 55-S compared to HCO^+ . We use HCO^+ as the primary clump tracer and further investigate various clump physical properties.

4.1. Clump column density

The molecular column density of the $\text{HCO}^+(1-0)$ transition at frequency ν is obtained by the assumption of Local Thermodynamic Equilibrium (LTE; Barnes et al. 2011; Mangum & Shirley 2015)

$$N = \frac{3h}{8\pi^3\mu_{lu}^2} \frac{Q_{\text{rot}}}{g_u} \exp\left(\frac{E_u}{kT_{\text{ex}}}\right) \left[\exp\left(\frac{h\nu}{kT_{\text{ex}}}\right) - 1 \right] \int \tau_{\nu} dV \quad (1)$$

Here μ_{lu} is the electric dipole matrix element which can be defined as $\mu_{lu} = S\mu^2$, where S is the line strength and μ is the dipole moment. Q_{rot} is the rotational partition function of the HCO^+ molecule,

$$Q_{\text{rot}} \equiv \sum_i g_i \exp\left(-\frac{E_i}{kT}\right) \quad (2)$$

where g is the degeneracy of the corresponding rotational level. E_u and g_u denote the energy and degeneracy of the upper molecular level respectively. T_{ex} is the excitation temperature and $\int \tau_{\nu} dV$ denotes the optical

depth of the emission line integrated over the velocity range.

The radiative transfer equation in the Rayleigh-Jeans limit can be written as

$$T_p = (T_{\text{ex}} - T_{\text{bg}})(1 - e^{-\tau}) \quad (3)$$

Here T_p is the peak brightness temperature of the emission line, and T_{bg} is the background temperature taken to be 2.72 K. The excitation temperature (T_{ex}) can be precisely determined if we have multiple transitions of HCO^+ , while our observation is limited to single transition. The excitation temperature T_{ex} of the cloud can also be estimated from optically thick $^{12}\text{CO} (1-0)$ transition. Naslim et al. (2018) determined the excitation temperature of the N 55-S molecular cloud using the $^{12}\text{CO} (1-0)$ transition (see Fig 4 of Naslim et al. 2018). Their study shows that T_{ex} values of $^{12}\text{CO} (1-0)$ range from 20 to 40 K in the N 55-S. We assume $T_{\text{ex}} = 30$ K as the excitation temperature of the $\text{HCO}^+(1-0)$ clumps in the N 55-S for further calculations. This value is consistent with the typical excitation temperature of molecular gas in massive clumps (Faúndez et al. 2004; Fontani et al. 2005). We obtain the peak optical depth (τ_p) from the peak brightness temperature of each clump using the equation (Barnes et al. 2011)

$$\tau_p = -\ln \left[1 - \frac{T_p}{(T_{\text{ex}} - T_{\text{bg}})} \right] \quad (4)$$

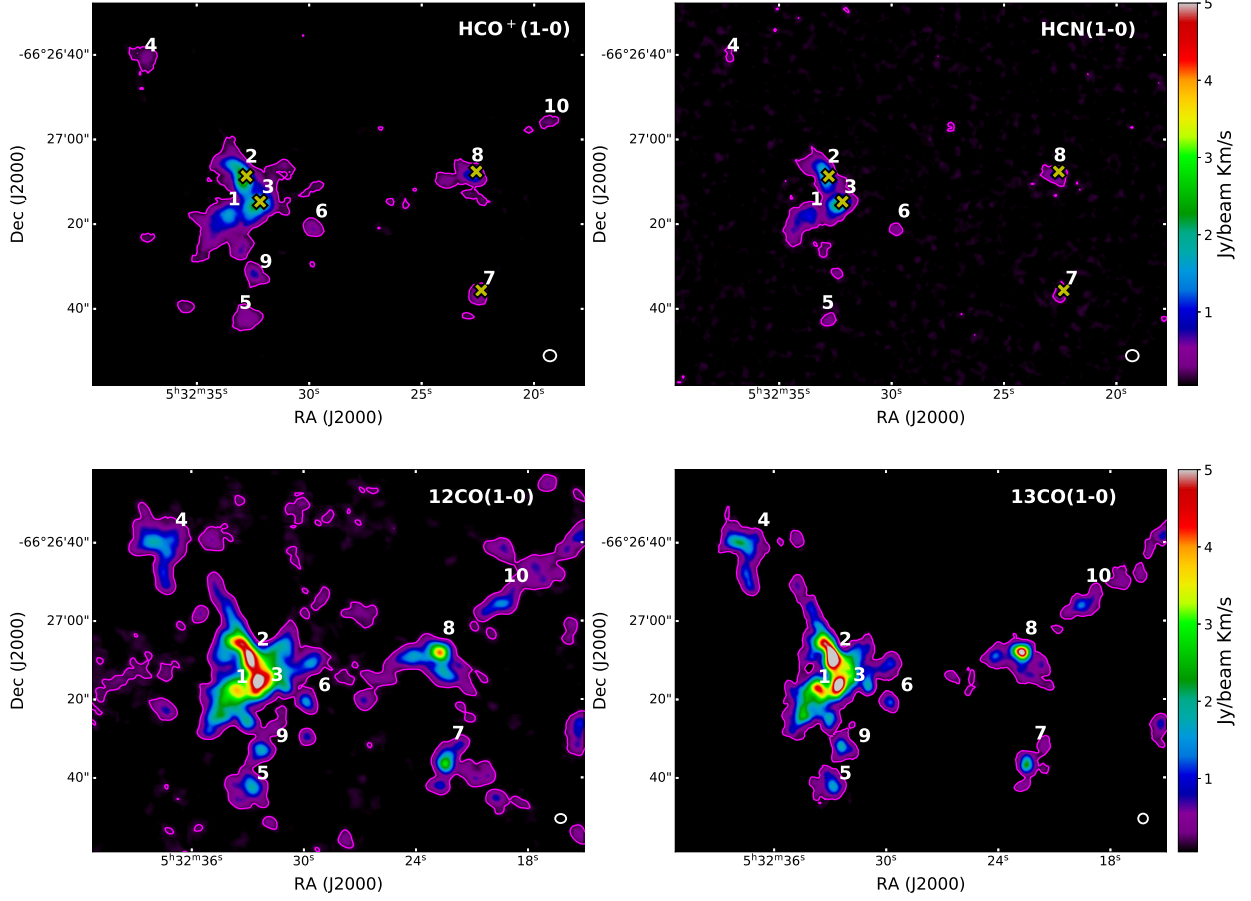


Figure 2. The velocity integrated intensity maps of HCO⁺(1−0) and HCN(1−0) emission of the N 55-S are shown along with ¹²CO(1−0) and ¹³CO(1−0) maps (Naslim et al. 2018) for comparison. The resolution of HCO⁺(1−0) and HCN(1−0) maps are 4.07×3.11 arcsec² and 4.13×3.14 arcsec² respectively. The numbers denote the identified clumps and the yellow cross symbols denote the positions of YSOs (Gruendl, & Chu 2009; Chen et al. 2009). The resolution of ¹²CO(1−0) map is 3.53×2.32 arcsec² and that of ¹³CO(1−0) map is 3.28×1.89 arcsec². The resolution elements are denoted in the bottom right corner of each map.

The peak brightness temperature T_p and optical depth τ_p of each clump are tabulated in Table 2. The partition function Q_{rot} of HCO⁺(1−0) transition is 14.4 at $T_{ex} = 30$ K (Rohlfs, & Wilson 2004; Mangum & Shirley 2015). Substituting for Q_{rot} , and taking $\int \tau_\nu dV = \tau_p \int \phi dV = \tau_p \sqrt{2\pi} \sigma_V$, equation 1 can be simplified as (Barnes et al. 2011),

$$N_p = 6.02 \times 10^{17} \tau_p \sqrt{2\pi} \sigma_V \text{ m}^{-2} \quad (5)$$

Here, we assume the emission line profiles, $\phi(V)$, to be Gaussian and σ_V denotes the velocity dispersion of the line in km s^{−1}. Assuming the relative abundance of HCO⁺ to H₂ to be $X=10^{-9}$ (Garrod et al. 2008; Loren et al. 1990; Caselli et al. 2002; Lee et al. 2003; Zinchenko et al. 2009), we derive the column density of molecular hydrogen (N_{H_2}). The estimated values of N_{H_2}

are tabulated in Table 2. Clumps which are truly at a higher T_{ex} will have lower N_p and viceversa. For $T_{ex} = 40$ K, the N_p values of the clumps are $\sim 28\%$ lower compared to the values derived for $T_{ex} = 30$ K and $\sim 39\%$ higher for $T_{ex} = 20$ K.

4.2. Clump volume density

The H₂ volume density (n_{col}) of each clump can be calculated assuming that the physical depth of the source is comparable to its projected size (Barnes et al. 2011).

$$n_{col} = \sqrt{\frac{\ln 2}{\pi}} \frac{N_p}{RX} \quad (6)$$

The above equation provides an average volume density through the clump along the peak of the emission line.

The derived clump volume densities range from 300 ± 50 to $4850 \pm 1630 \text{ cm}^{-3}$ (Table 2). $\text{HCO}^+(1-0)$ is expected to be thermalized at a critical density of $n_{\text{cr}} \sim 3 \times 10^5 \text{ cm}^{-3}$ (Barnes, & Crutcher 1990). The $\text{HCO}^+(1-0)$ line emission towards all the clumps in our sample is excited well below the critical density.

4.3. Mass surface density

We estimate the total mass surface density (Σ_p) of molecular clumps using the $\text{HCO}^+(1-0)$ column densities (Barnes et al. 2011)

$$\Sigma_p = \left(\frac{N_p}{X} \right) (\mu_{\text{mol}} m_H) \quad (7)$$

where μ_{mol} is the mean molecular weight in the gas which is taken to be 2.3 (Barnes et al. 2011). The calculated mass-surface density of all identified clumps of N 55-S are given in Table 2. The values of mass-surface density vary from 29 ± 4 to $290 \pm 41 M_\odot \text{ pc}^{-2}$.

4.4. Mass of molecular clumps

The masses of molecular clumps (M_{LTE}) are calculated from the derived $\text{HCO}^+(1-0)$ column densities under the LTE assumption.

$$M_{\text{LTE}} = \frac{N_p}{X} (\mu_{\text{mol}} m_H) \pi R^2 \quad (8)$$

We also determine the clump virial masses (Larson 1981; Solomon et al. 1987; Saito et al. 2006; Wong et al. 2006; Muller et al. 2010) using the equation,

$$M_{\text{vir}} = 125 M_\odot \frac{(5 - 2\beta)}{(3 - \beta)} \Delta v^2 R \quad (9)$$

This equation is based on the assumption that clumps are spherical in shape with a radial power-law density profile of index β . we assume $\beta = 1$ (van der Tak et al. 2000). R is the clump radius in parsec and Δv is the FWHM of the emission line in km s^{-1} . The M_{LTE} and M_{vir} masses of the clumps, as well as the virial parameter, $\alpha = M_{\text{vir}}/M_{\text{LTE}}$, are tabulated in Table 2.

5. PHYSICAL PROPERTIES OF DENSE MOLECULAR GAS

We investigate the physical properties of the dense molecular clumps of N 55-S in the LMC, traced by ALMA observations of $\text{HCO}^+(1-0)$ and $\text{HCN}(1-0)$ emission. In Fig 2, we compare the velocity integrated intensity maps of $^{12}\text{CO}(1-0)$ and $^{13}\text{CO}(1-0)$ (Naslim et al. 2018) with $\text{HCO}^+(1-0)$ and $\text{HCN}(1-0)$ of the N 55-S region. The spatial distribution of the emission from all four molecular transitions are broadly

similar. The maximum intensity in all four emission maps comes from clumps 2 and 3. The $^{13}\text{CO}(1-0)$, $\text{HCO}^+(1-0)$ and $\text{HCN}(1-0)$ emission are not detected in regions of weak $^{12}\text{CO}(1-0)$ emission. It is evident that $^{12}\text{CO}(1-0)$ emission is more widely spread compared to $^{13}\text{CO}(1-0)$, $\text{HCO}^+(1-0)$ and $\text{HCN}(1-0)$. The distribution of the $\text{HCO}^+(1-0)$ and $\text{HCN}(1-0)$ emission is most compact. The projected spatial distribution of emission from multiple species reflects the density structure of the molecular clumps from surface to the interior.

5.1. Dense gas fraction

We estimate the H_2 mass traced by $^{12}\text{CO}(1-0)$ (Naslim et al. 2018) luminosities (L_{CO}) from the N 55-S region using the equation (Wong et al. 2011).

$$M_{\text{H}_2}[M_\odot] = 4.4 \frac{X_{\text{CO}}}{2.2 \times 10^{20} \text{ cm}^{-2} (\text{K km s}^{-1})} L_{\text{CO}} (\text{K km s}^{-1} \text{ pc}^2) \quad (10)$$

Here X_{CO} denotes the CO-to- H_2 conversion factor which has a Galactic value, $X_{\text{CO}} = 2 \times 10^{20} \text{ cm}^{-2} \text{ K}^{-1} \text{ km}^{-1} \text{ s}$ (Strong et al. 1988; Bolatto et al. 2013). Both theoretical and observational studies suggest that X_{CO} value increases with decreasing metallicity. However, a Galactic value can be approximated for environments with metallicities down to $\sim 0.5 Z_\odot$ (Leroy et al. 2011; Bolatto et al. 2013; Pineda et al. 2017). Hence we use $X_{\text{CO}} = 2 \times 10^{20} \text{ cm}^{-2} \text{ K}^{-1} \text{ km}^{-1} \text{ s}$ in our calculation. Naslim et al. (2018) report a 30% missing flux in the ALMA $^{12}\text{CO}(1-0)$ emission maps. Accounting for this, the total H_2 mass traced by $^{12}\text{CO}(1-0)$ is $(2.59 \pm 0.01) \times 10^4 M_\odot$. The total H_2 mass traced by $\text{HCO}^+(1-0)$ is $\sim (0.70 \pm 0.10) \times 10^3 M_\odot$ (sum of $M_{\text{LTE}}/\mu_{\text{mol}}$ in Table 2). Thus the dense gas fraction in the N 55-S region is 0.025 ± 0.005 . A higher value of $X_{\text{CO}} = 4 \times 10^{20} \text{ cm}^{-2} \text{ K}^{-1} \text{ km}^{-1} \text{ s}$ (Hughes et al. 2010) will further decrease the dense gas fraction to 0.013.

5.2. Low volume densities of dense gas clumps

The volume densities of ten identified clumps are in a range $(0.30 - 4.85) \times 10^3 \text{ cm}^{-3}$ (Table 2). Since $\text{HCO}^+(1-0)$ has a relatively high critical density $\sim 3 \times 10^5 \text{ cm}^{-3}$ (Barnes, & Crutcher 1990), we would expect the bulk of $\text{HCO}^+(1-0)$ luminosity to originate in thermalized star-forming cores. However, all ten HCO^+ clumps in our samples show volume densities well below the expected critical density. We note that similar low volume densities are reported for Milky Way clouds from $\text{HCO}^+(1-0)$ emission (Barnes et al. 2011). The authors report that 95% of all massive clumps emit well below the critical density. A study of $\text{HCO}^+(1-0)$ emission from multiple clouds of the LMC also suggests that

Table 1. Details of the clumps identified by astrodendro

ID	RA	Dec	R	σ_v	$F_{\text{HCN}}/$	YSO
No	(deg)	(deg)	(pc)	(km s ⁻¹)	F_{HCO^+}	association
1	83.1406	-66.4551	0.56±0.14	0.43±0.10	0.78±0.12	No
2	83.1374	-66.4523	0.49±0.15	0.86±0.12	0.60±0.08	Yes
3	83.1343	-66.4541	0.48±0.19	0.67±0.13	0.77±0.15	Yes
4	83.1560	-66.4450	1.11±0.07	0.62±0.05	0.58±0.07	No
5	83.1385	-66.4617	0.68±0.12	0.53±0.09	0.51±0.09	No
6	83.1244	-66.4557	0.41±0.19	0.48±0.19	0.46±0.17	No
7	83.0933	-66.4601	0.79±0.10	0.94±0.07	0.54±0.12	Yes
8	83.0955	-66.4526	1.12±0.07	1.02±0.04	0.53±0.08	Yes
9	83.1347	-66.4592	0.85±0.11	0.62±0.07	–	No
10	83.0821	-66.4490	0.79±0.10	0.54±0.08	–	No

NOTE— R and σ_v denotes the radius and velocity dispersion of each clump derived from astrodendro. F_{HCO^+} and F_{HCN} are the flux densities of HCO⁺(1–0) and HCN(1–0) clumps respectively.

Table 2. Properties of HCO⁺(1–0) clumps.

ID	Δv	T_p	τ_p	M_{vir}	N_{H_2}	M_{LTE}	Σ_p	n_{col}	α
No	(km s ⁻¹)	(K)	-	(×10 ² M _⊙)	(×10 ²¹ cm ⁻²)	(×10 ² M _⊙)	(×10 ² M _⊙ pc ⁻²)	(×10 ³ cm ⁻³)	($M_{\text{vir}}/M_{\text{LTE}}$)
1	1.01±0.24	2.75	0.10	1.07 ± 0.57	6.85 ± 1.66	1.24 ± 0.67	1.26 ± 0.31	1.87 ± 0.64	0.86 ± 0.66
2	2.03±0.29	3.10	0.12	3.82 ± 1.59	15.71 ± 2.22	2.22 ± 1.39	2.90 ± 0.41	4.85 ± 1.63	1.73 ± 1.30
3	1.58±0.30	3.46	0.13	2.26 ± 1.22	13.76 ± 2.61	1.84 ± 1.46	2.54 ± 0.48	4.36 ± 1.87	1.23 ± 1.18
4	1.45±0.12	0.71	0.03	4.35 ± 0.79	2.43 ± 0.21	1.72 ± 0.27	0.45 ± 0.04	0.33 ± 0.03	2.53 ± 0.61
5	1.26±0.20	1.52	0.06	2.03 ± 0.74	4.62 ± 0.75	1.25 ± 0.48	0.85 ± 0.14	1.03 ± 0.24	1.62 ± 0.85
6	1.12±0.45	1.66	0.06	0.96 ± 0.90	4.51 ± 1.82	0.43 ± 0.45	0.83 ± 0.33	1.69 ± 1.05	2.22 ± 3.11
7	2.20±0.16	0.75	0.03	7.20 ± 1.39	3.95 ± 0.28	1.43 ± 0.38	0.73 ± 0.05	0.76 ± 0.11	5.04 ± 1.66
8	2.40±0.10	1.02	0.04	12.16 ± 1.29	5.86 ± 0.24	4.29 ± 0.59	1.08 ± 0.04	0.79 ± 0.06	2.84 ± 0.49
9	1.46±0.17	0.66	0.02	3.43 ± 0.92	2.30 ± 0.27	0.97 ± 0.27	0.42 ± 0.05	0.41 ± 0.07	3.53 ± 1.37
10	1.26±0.19	0.52	0.02	2.36 ± 0.76	1.57 ± 0.23	0.56 ± 0.16	0.29 ± 0.04	0.30 ± 0.05	4.19 ± 1.82

NOTE— Δv denotes the FWHM of the HCO⁺(1–0) emission line. T_p is the peak brightness temperature and τ_p is the corresponding optical depth. M_{vir} denotes the virial masses of each clump. N_{H_2} denotes the column density of molecular hydrogen in each clump which is related to HCO⁺ column density (N_p) as $N_{\text{H}_2} = N_p \times 10^9$. M_{LTE} and Σ_p denotes the LTE masses and the total mass surface density of each clump respectively. n_{col} denotes volume number density of molecular hydrogen in each clump and α represents the virial ratio defined as $M_{\text{vir}}/M_{\text{LTE}}$. The values are estimated assuming $T_{\text{ex}} = 30$ K. The uncertainties due to the assumption of T_{ex} described in 4.1 are not included in the errors here.

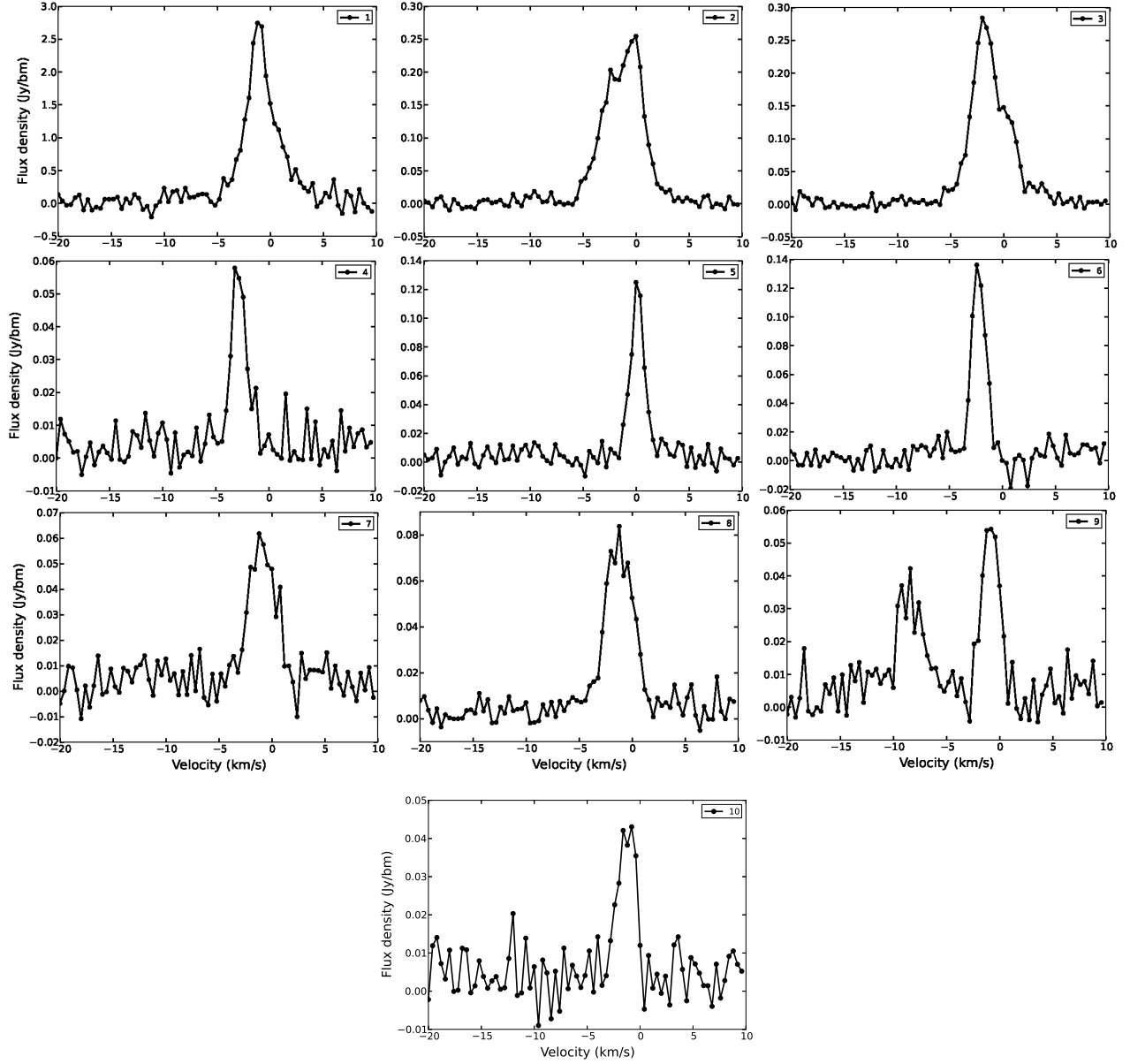


Figure 3. The HCO⁺(1 – 0) emission spectra of 10 molecular clumps of the N 55-S. We note an additional red-shifted feature in the spectrum of clump 9, possibly due to any dynamical activity in this region.

the majority of the clumps have volume densities² well below the critical density of $J = 1 - 0$ line (Seale et al. 2012).

This could happen if HCO⁺(1 – 0) is sub-thermally excited and not thermalized to the local H₂ gas. Significant HCO⁺(1 – 0) emission can arise at densities lower than the critical density of the line (Evans 1999; Shirley 2015; Kauffmann, et al. 2017). Another possibility is a severe underestimation of optical depth of the emission line due to small beam filling factor. The clump mass can be calculated assuming that the clump volume contains gas at the critical density of the HCO⁺(1 – 0) transition (Barnes et al. 2011).

$$M = 5.3 \times f \left(\frac{n_{\text{cr}}}{10^{11} \text{m}^{-3}} \right) \left(\frac{R}{\text{pc}} \right)^3 \quad (11)$$

Here n_{cr} denotes the critical density of HCO⁺(1 – 0) and f denotes the beam filling factor. Comparing the above derived mass with the cloud mass derived from LTE analysis yields $f = (0.001 - 0.01)$ for the clumps in our sample. This low beam filling factor could result from a highly clumpy structure of molecular clouds or if the clumps are not well resolved.

5.3. M_{vir} versus M_{LTE}

The virial and LTE masses of N 55-S clumps are $(0.96 - 12.16) \times 10^2 M_{\odot}$ and $(0.43 - 4.29) \times 10^2 M_{\odot}$ respectively (see Fig 4A). In order to examine whether these clumps are gravitationally bound, we inspect the virial parameter; $\alpha = M_{\text{vir}}/M_{\text{LTE}}$ (Fig 4B). The average value of virial parameter is 2.6 ± 1.2 . A few isolated clumps such as 4, 6, 7, 8, 9 and 10 are not likely to be gravitationally bound. The relatively high value of virial parameter could be due to an underestimation of M_{LTE} in these region or due to dynamical impact of star formation.

5.4. size-linewidth relation

The size and linewidth of HCO⁺(1 – 0) clumps follow a power-law, $\Delta v \propto R^{0.65 \pm 0.32}$ (Fig 4C). The size-linewidth relation of ¹²CO(1 – 0) clumps of the N 55 is $\Delta v \propto R^{0.4}$ (Naslim et al. 2018). The size-linewidth power-law index is found to be in the range 0.46 – 0.78 for several dense gas tracers in the central molecular zone (CMZ) of the Milky Way (Shetty et al. 2012). The slope is found to be 0.6 in extragalactic clouds (Bolatto et al. 2008) and 0.5 in Milky Way clouds (Heyer et al. 2009). Thus the size-linewidth power-law index of HCO⁺(1 – 0)

clumps of the N 55-S is consistent with the CMZ, extragalactic, and the Milky Way clouds.

6. CLUMP ASSOCIATION WITH YSOS

There exist extensive catalogues of YSOs in the LMC due to its proximity and the ability to observe the entire galaxy (Whitney et al. 2008; Gruendl, & Chu 2009; Indebetouw et al. 2004; Chen et al. 2009, 2010; Ellingsen et al. 2010). This gives the advantage of positional matching the YSOs with dense molecular clumps to study star formation and the associated dense gas. In Fig 2, we mark the position of YSOs in the N 55-S (Gruendl, & Chu 2009; Chen et al. 2009) on top of the velocity integrated intensity maps of HCO⁺(1 – 0) and HCN(1 – 0). All 4 identified YSOs in the N 55-S are near the HCO⁺(1 – 0) and HCN(1 – 0) emission peaks (near clumps 2, 3, 7 and 8). The positional offset between the emission peak and YSO position is 1.16, 1.21, 0.43 and 1.69 arcsec for clump 2, 3, 7, and 8 respectively. If the YSOs are randomly distributed, the probability of a YSO locating within 2 arcsec of an emission peak is only 0.04%. However, all 4 of the identified YSOs are near the emission peaks indicating their positions are not from a random distribution and are related to the dense molecular clumps. The young stars form in the densest cores of the molecular clouds (Krumholz et al. 2010). The YSOs that are at significant offset from the emission peak of the molecular clumps are expected to be slightly evolved than those at the core. This hypothesis is observationally supported by the detection of maser emission (sign of early phase of YSO evolution) in 80% of YSOs located close to the emission peaks of molecular clouds (Seale et al. 2012). Thus the YSOs associated to clump 2, 3, 7, and 8 in the N 55-S are likely to be early in their evolutionary stage.

Gruendl, & Chu (2009) suggest that the 8 μ m magnitude of YSOs can be treated as a good proxy of the YSO mass based on the radiation transfer models on the spectral energy distribution (SED) of various YSOs. The YSOs with 8 μ m magnitude brighter than [8.0] are classified as massive YSOs. The infrared SED fitting of various YSOs in the N 44, and N 159 shows YSO mass of 8–15 M_{\odot} for 8 μ m magnitudes \sim [8.76], [8.94], [8.24]. The masses are \sim 5–10 M_{\odot} for 8 μ m magnitude \sim [10.17] (Table 7 of Chen et al. 2009). The 8 μ m magnitudes of the YSOs associated with clumps 2, 3, 7, and 8 in the N 55-S are \sim [8.24], [7.27], [10.19] and [8.76] respectively (Gruendl, & Chu 2009). Thus the YSOs associated to clump 2, 3, and 8 are likely to be massive (8–15 M_{\odot}) and associated to clump 7 could be of mass \sim (5–10) M_{\odot} .

² We computed the volume densities from the M_{LTE} and R values from Table 2 of (Seale et al. 2012).

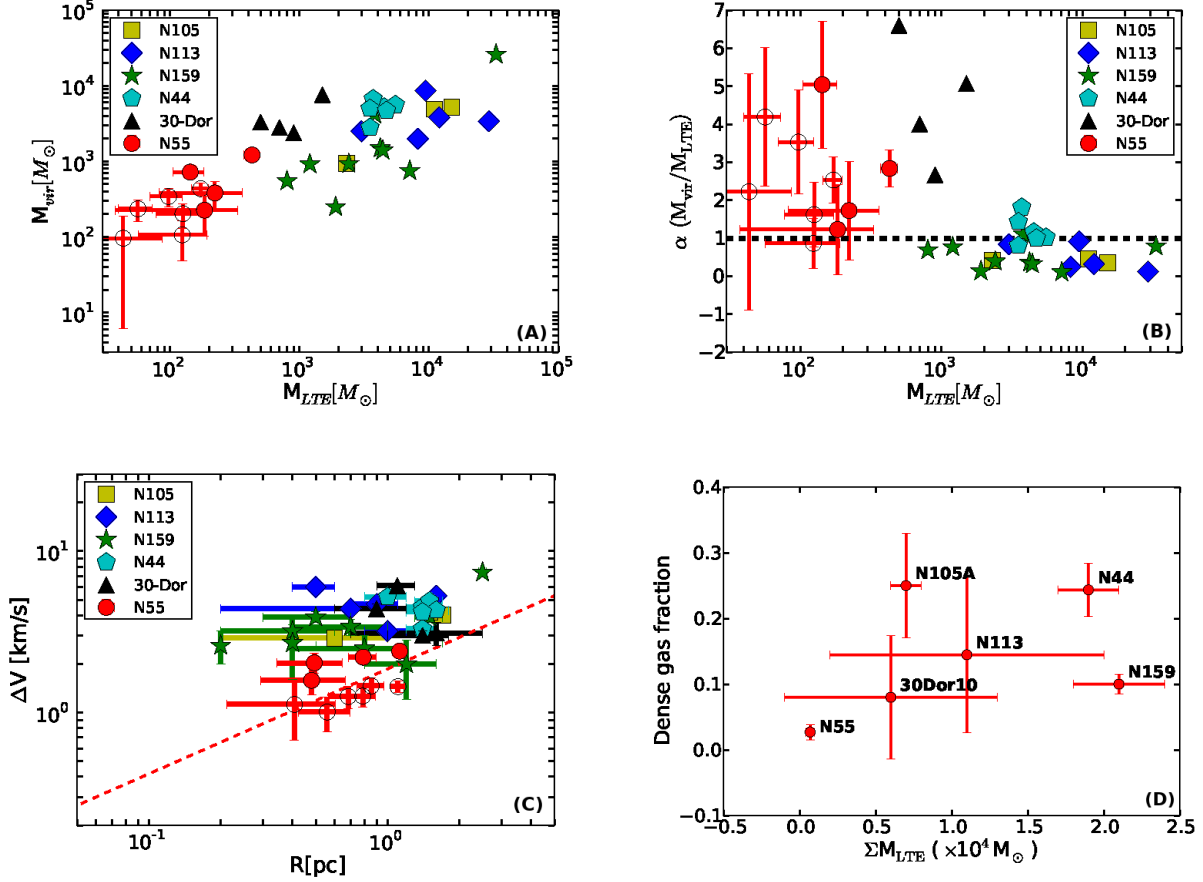


Figure 4. (A) Virial versus LTE masses plot of $\text{HCO}^+(1-0)$ molecular clumps in N 55-S (this work) along with clumps in other LMC GMCs N 105, N 113, N 159, N 44 (Seale et al. 2012) and 30 Doradus-10 (Anderson et al. 2014). (B) M_{LTE} versus virial parameter (α) for the N 55-S $\text{HCO}^+(1-0)$ clumps together with other GMCs of the LMC (Seale et al. 2012; Anderson et al. 2014). (C) The size versus linewidth relation for $\text{HCO}^+(1-0)$ clumps (red circles) in N 55-S clumps fitted with a power-law, $\Delta v \propto R^{0.65 \pm 0.32}$ (red dotted line). The R and Δv values of $\text{HCO}^+(1-0)$ clumps in other GMCs of the LMC (Seale et al. 2012; Anderson et al. 2014) are shown for comparison. The closed circles denote the clumps with associated YSOs and the open circles denote those without YSOs in panels A, B, and C. (D) The total molecular gas mass traced by $\text{HCO}^+(1-0)$ under the assumption of LTE versus the dense gas mass fraction for N 55-S and other GMCs of the LMC (Seale et al. 2012; Anderson et al. 2014).

We compare the physical properties of the clumps in light of the presence/absence of YSOs. The molecular clumps with YSOs in our sample are relatively massive than those without YSOs. The average mass of the YSO-associated clumps is $245 \pm 96 M_{\odot}$ whereas the average mass of clumps without YSOs is $\sim 103 \pm 39 M_{\odot}$. Similar lines of observational evidence are reported for various regions of the LMC (Seale et al. 2012; Naslim et al. 2018) and for the Milky Way molecular clumps (Hill et al. 2005). The clumps with mass-surface densities $\geq 73 M_{\odot} \text{ pc}^{-2}$ shows YSO association in N 55-S. The mass surface density threshold of clumps for massive star formation is $\sim 501 M_{\odot} \text{ pc}^{-2}$ and $794 M_{\odot} \text{ pc}^{-2}$ for N 159W and N 159E respectively (Nayak et al. 2018). The star formation threshold for 30-Doradus is $\sim 670 M_{\odot} \text{ pc}^{-2}$ (Nayak et al. 2016). Thus the mass density

threshold of N 159 and 30-Doradus is (6-10) times higher compared to N 55-S. This could be due to the relatively less extreme star-forming environment of N 55-S. The stronger radiation field in the N 159 and 30-Doradus is possibly preventing massive star formation at low mass surface density in these regions.

We also find the velocity widths of YSO-bearing clumps to be systematically larger than those of non-YSO associated clumps. The velocity widths of YSO associated clumps are $\Delta v = 1.6 - 2.4 \text{ km s}^{-1}$ whereas the clumps without YSOs, $\Delta v = 1.0 - 1.5 \text{ km s}^{-1}$. The larger linewidths could be indicative of turbulence due to YSO activity, indicating that YSOs affect the properties of dense molecular clumps. These results are consistent with the $^{13}\text{CO}(1-0)$ and $^{12}\text{CO}(1-0)$ study of the N 55 region (Naslim et al. 2018). Similar results are reported

for ¹²CO(2–1) study of 30 Doradus (Nayak et al. 2016), ¹²CO/¹³CO observations of N159W/E (Fukui et al. 2019; Tokuda et al. 2019) and HCO⁺(1–0) study of several GMCs of the LMC (Seale et al. 2012).

7. COMPARISON OF N 55 CLUMP PROPERTIES WITH OTHER LMC CLOUDS

Seale et al. (2012) studied molecular clumps of different star forming GMCs of the LMC (N159, N105A, N44, and N113) using dense gas tracers HCO⁺(1–0) and HCN(1–0). The authors used ATCA observations with a spatial resolution of $\sim 6 \times 7$ arcsec² ($\sim 1.4 \times 1.7$ pc² in linear scale) and a spectral resolution of ~ 0.2 km s^{−1} (for N105 and N113); 0.4 km s^{−1} (N159 and N44). A similar study of dense gas tracers at same spatial resolution was carried out by Anderson et al. (2014) in the 30 Doradus-10 with a spectral resolution of 0.84 km s^{−1}. We examine the molecular clump properties such as size, linewidth, mass and dense gas fraction of N55-S region in comparison to other GMCs of the LMC in Fig 4.

The size of clumps in N55-S is comparable to the clumps of other GMCs (see Fig 4C). However, the linewidths of the N55-S clumps are slightly small compared to other regions of the LMC (Anderson et al. 2014; Seale et al. 2012). The small linewidths could be indicative of relatively less energetic environmental conditions in the N55-S. We compare the clump masses (both virial and LTE) of N55-S with other star forming regions of the LMC (Seale et al. 2012) in Fig 4A. The M_{vir} and M_{LTE} derived for N55-S clumps are systematically lower than other regions of the LMC. A few of the dense molecular clumps of N55-S are likely not in gravitational equilibrium.

The molecular gas mass traced by the HCO⁺(1–0) clumps versus dense gas fraction for N55-S and other GMCs (Seale et al. 2012; Anderson et al. 2014) in the LMC are shown in Fig 4D. The dense gas fraction of N55-S is 0.025 ± 0.005 , smaller than the fraction seen in other GMCs; 0.1 – 0.24 . Dense gas fraction is crucial for massive star formation and is directly proportional to the star formation efficiency within a GMC (Krumholz et al. 2012; Lada et al. 2012). This suggests that N55-S has lower star formation efficiencies compared to other GMCs of the LMC. However, we note that different dynamical environments of galaxies and stellar feedback play crucial role in setting massive star formation efficiency (Querejeta et al. 2019; Ochsendorf et al. 2017).

The HCN/HCO⁺ flux ratio of molecular clumps in the N55-S range from 0.46 ± 0.17 to 0.78 ± 0.12 . HCN and HCO⁺ molecules possess similar rotational constants

and electric dipole moments. Hence the higher flux ratio can be attributed to the relative abundance. However we note that a strong UV radiation field due to high star formation activity can enhance the HCO⁺ abundance in active star forming regions (Meijerink et al. 2011; Bayet et al. 2011). The HCN/HCO⁺ flux ratio is found to be $(0.1$ – $0.5)$ for various LMC clouds (N105, N113, N159, and N44) by Seale et al. (2012) and ~ 0.2 for 30 Doradus-10 by Anderson et al. (2014) at similar spatial resolution. Thus N55-S clumps possess relatively high flux ratio compared to other GMCs in the LMC possibly due to the low radiation field compared to other GMCs.

There exist HCN/HCO⁺ flux ratio measurements of various LMC clouds using single dish observations in the literature (Nishimura et al. 2016; Chin et al. 1997). These authors report the flux ratios in the range $(0.5$ – $0.7)$ for various molecular clouds of the LMC (N113, N44BC, N159HW, N214DE, N159W). These numbers are slightly higher than their respective values at high spatial resolution (parsec scale; Seale et al. 2012; Anderson et al. 2014) as mentioned above. The flux ratio from single dish observations reflect the chemical composition pattern averaged over a molecular cloud scale of 10 – 14 pc where the effect of local star formation activity is smeared out. The parsec scale observations probe individual dense star forming clumps and need not be same with the flux ratio averaged over 10 – 14 pc. The higher HCN/HCO⁺ ratios with single-dish data imply that the variation in abundance has a greater impact on the ratio than in density.

8. SUMMARY

We present high spatial resolution observations of HCO⁺(1–0) and HCN(1–0) of the N55-S region in the LMC. We aim to compare the the dense molecular clump properties of the N55-S with other active star forming regions (N159 and 30-Doradus) in order to understand the effect of different feedback environment on dense molecular clumps. We detect prominent HCO⁺(1–0) emission from 10 clumps and HCN(1–0) emission from 8 clumps. Our main results are the following:

1. The column density of H₂ gas traced by HCO⁺(1–0) emission in N55-S clumps are in the range $N_{\text{H}_2} \sim (0.2$ – $1.6) \times 10^{22}$ cm^{−2}. The LTE mass and mass-surface density of the clumps are in the range $M_{\text{LTE}} \sim (0.4$ – $4.3) \times 10^2 M_{\odot}$ and $\Sigma_p \sim (0.3$ – $2.9) \times 10^2 M_{\odot}$ pc^{−2} respectively.
2. The volume density of H₂ gas is in the range $n_{\text{col}} \sim (0.3$ – $4.9) \times 10^3$ cm^{−3}; less than critical density of HCO⁺(1–0) emission line suggesting that

the clouds are either sub-thermally excited or have very small beam filling factors.

3. The size-linewidth relation of $\text{HCO}^+(1-0)$ clumps follow a power-law with index 0.65 ± 0.32 , similar to CMZ, several extragalactic and Galactic clouds which is consistent with the ^{12}CO clumps (Naslim et al. 2018).
4. All four identified YSOs in the N 55-S region are in the vicinity of $\text{HCO}^+(1-0)$ and $\text{HCN}(1-0)$ emission peaks indicating the association of these dense clumps with recent star formation. The YSO associated clumps have relatively larger linewidths and masses compared to those without YSOs.
5. The total H_2 mass traced by $^{12}\text{CO}(1-0)$ and $\text{HCO}^+(1-0)$ in the N 55-S region is $2.59 \times 10^4 M_\odot$, and $0.70 \times 10^3 M_\odot$ respectively, indicating a dense gas fraction of 0.025 ± 0.005 . The dense gas fraction of N 55-S is lower compared to other GMCs (N 105, N 113, N 159, N 44, and 30-Doradus) of the LMC indicating a relatively lower SFE.
6. The HCN/HCO^+ flux ratio of N 55-S is in the range 0.46 ± 0.17 to 0.78 ± 0.12 , slightly higher than the ratio (0.1 – 0.5) seen in other GMCs like N 105, N 113, N 159, N 44, and 30-Doradus (Seale et al. 2012; Anderson et al. 2014). We in-

terpret this to be an effect of relatively low radiation field and star formation activity in the N 55-S.

7. The N 55-S clumps possess systematically lower linewidths compared to other GMCs of the LMC (Seale et al. 2012; Anderson et al. 2014). We also note that the YSO associated clumps of N 55-S show mass-surface density $\geq 73 M_\odot \text{pc}^{-2}$ which is (6-10) times lower compared to N 159 (Nayak et al. 2018) and 30-Doradus (Nayak et al. 2016).

Our study of the dense molecular clumps in N 55-S suggests that YSOs can significantly affect the properties of dense molecular clumps by increasing the linewidths of molecular emission. Compared to other GMCs in the LMC, the dense molecular clumps of N 55-S show smaller linewidths, lower dense gas fraction, larger HCN/HCO^+ , and smaller threshold of mass surface density with YSOs indicating relatively less active star formation.

ACKNOWLEDGMENTS

This paper makes use of the following ALMA data: ADS/JAO.ALMA #2013.1.00993.S. ALMA is a partnership of the ESO, NSF, NINS, NRC, NSC, and ASIAA. The Joint ALMA Observatory is operated by the ESO, AUI/NRAO, and NAOJ. This research has been supported by United Arab Emirates University, under start-up grant number 31S378. This research has been supported by the Ministry of Science and Technology of Taiwan, under grant MOST107-2119-M-001-031-MY3 and Academia Sinica under grant AS-IA-106-M03.

REFERENCES

- Ambrocio-Cruz, P., Laval, A., Marcelin, M., et al. 1998, *A&A*, 339, 173
- Anderson, C. N., Meier, D. S., Ott, J., et al. 2014, *ApJ*, 793, 37
- Barnes, P. J., & Crutcher, R. M. 1990, *ApJ*, 351, 176
- Barnes, P. J., Yonekura, Y., Fukui, Y., et al. 2011, *ApJS*, 196, 12
- Bayet, E., Viti, S., Hartquist, T. W., et al. 2011, *MNRAS*, 417, 627
- Bolatto, A. D., Leroy, A. K., Rosolowsky, E., et al. 2008, *ApJ*, 686, 948
- Bolatto, A. D., Wolfire, M., & Leroy, A. K. 2013, *ARA&A*, 51, 207
- Carlson, L. R., Sewilo, M., Meixner, M., et al. 2012, *A&A*, 542, A66
- Caselli, P., Walmsley, C. M., Zucconi, A., et al. 2002, *ApJ*, 565, 344
- Chen, C.-H. R., Chu, Y.-H., Gruendl, R. A., et al. 2009, *ApJ*, 695, 511
- Chen, C.-H. R., Indebetouw, R., Chu, Y.-H., et al. 2010, *ApJ*, 721, 1206
- Chin, Y.-N., Henkel, C., Whiteoak, J. B., et al. 1997, *A&A*, 317, 548
- Draine, B. T. 1978, *ApJS*, 36, 595
- Ellingsen, S. P., Breen, S. L., Caswell, J. L., et al. 2010, *MNRAS*, 404, 779
- Evans, N. J. 1999, *ARA&A*, 37, 311
- Faúndez, S., Bronfman, L., Garay, G., et al. 2004, *A&A*, 426, 97
- Fontani, F., Beltrán, M. T., Brand, J., et al. 2005, *A&A*, 432, 921

- Fukui, Y., Harada, R., Tokuda, K., et al. 2015, *ApJL*, 807, L4
- Fukui, Y., Tokuda, K., Saigo, K., et al. 2019, *ApJ*, 886, 14
- Garrod, R. T., Widicus Weaver, S. L., & Herbst, E. 2008, *ApJ*, 682, 283
- Gruendl, R. A., & Chu, Y.-H. 2009, *ApJS*, 184, 172
- Heyer, M., Krawczyk, C., Duval, J., et al. 2009, *ApJ*, 699, 1092
- Hill, T., Burton, M. G., Minier, V., et al. 2005, *MNRAS*, 363, 405
- Hughes, A., Wong, T., Ott, J., et al. 2010, *MNRAS*, 406, 2065
- Indebetouw, R., Johnson, K. E., & Conti, P. 2004, *AJ*, 128, 2206
- Indebetouw, R., Brogan, C., Chen, C.-H. R., et al. 2013, *ApJ*, 774, 73
- Indebetouw, R., Wong, T., Chen, C.-H. R., et al. 2020, *ApJ*, 888, 56
- Kauffmann J., Goldsmith P. F., Melnick G., Tolls V., Guzman A., Menten K. M., 2017, *A&A*, 605, L5
- Kennicutt, R. C., & Evans, N. J. 2012, *ARA&A*, 50, 531
- Krumholz, M. R., Cunningham, A. J., Klein, R. I., et al. 2010, *ApJ*, 713, 1120
- Krumholz, M. R., Dekel, A., & McKee, C. F. 2012, *ApJ*, 745, 69
- Lada, C. J., Forbrich, J., Lombardi, M., et al. 2012, *ApJ*, 745, 190
- Larson, R. B. 1981, *MNRAS*, 194, 809
- Lee, J.-E., Evans, N. J., Shirley, Y. L., et al. 2003, *ApJ*, 583, 789
- Leroy, A. K., Bolatto, A., Gordon, K., et al. 2011, *ApJ*, 737, 12
- Loren, R. B., Wootten, A., & Wilking, B. A. 1990, *ApJ*, 365, 269
- Mangum, J. G. & Shirley, Y. L. 2015, *PASP*, 127, 266
- McMullin, J. P., Waters, B., Schiebel, D., et al. 2007, *Astronomical Data Analysis Software and Systems XVI*, 127
- Meijerink, R., Spaans, M., Loenen, A. F., et al. 2011, *A&A*, 525, A119
- Meixner, M., Galliano, F., Hony, S., et al. 2010, *A&A*, 518, L71
- Muller, E., Ott, J., Hughes, A., et al. 2010, *ApJ*, 712, 1248
- Naslim, N., Kemper, F., Madden, S. C., et al. 2015, *MNRAS*, 446, 2490
- Naslim, N., Tokuda, K., Onishi, T., et al. 2018, *ApJ*, 853, 175
- Nayak, O., Meixner, M., Indebetouw, R., et al. 2016, *ApJ*, 831, 32
- Nayak, O., Meixner, M., Fukui, Y., et al. 2018, *ApJ*, 854, 154
- Nishimura, Y., Shimonishi, T., Watanabe, Y., et al. 2016, *ApJ*, 818, 161
- Ochsendorf, B. B., Meixner, M., Roman-Duval, J., et al. 2017, *ApJ*, 841, 109
- Olsen, K. A. G., Kim, S., & Buss, J. F. 2001, *AJ*, 121, 3075
- Pietrzyński, G., Graczyk, D., Gallenne, A., et al. 2019, *Nature*, 567, 200
- Pineda, J. L., Ott, J., Klein, U., et al. 2009, *ApJ*, 703, 736
- Pineda, J. L., Langer, W. D., Goldsmith, P. F., et al. 2017, *ApJ*, 839, 107
- Querejeta, M., Schinnerer, E., Schrubba, A., et al. 2019, *A&A*, 625, A19
- Retes-Romero, R., Mayya, Y. D., Luna, A., et al. 2017, *ApJ*, 839, 113
- Rohlfs, K., & Wilson, T. L. 2004, *Tools of radio astronomy*
- Rosolowsky, E. W., Pineda, J. E., Kauffmann, J., et al. 2008, *ApJ*, 679, 1338
- Saito, H., Saito, M., Moriguchi, Y., et al. 2006, *PASJ*, 58, 343
- Seale, J. P., Looney, L. W., Wong, T., et al. 2012, *ApJ*, 751, 42
- Seale, J. P., Meixner, M., Sewilo, M., et al. 2014, *AJ*, 148, 124
- Shetty, R., Beaumont, C. N., Burton, M. G., et al. 2012, *MNRAS*, 425, 720
- Shirley Y. L., 2015, *PASP*, 127, 299
- Smith, R. C., & MCELS Team 1998, *PASA*, 15, 163
- Solomon, P. M., Rivolo, A. R., Barrett, J., et al. 1987, *ApJ*, 319, 730
- Strong, A. W., Bloemen, J. B. G. M., Dame, T. M., et al. 1988, *A&A*, 207, 1
- Tokuda, K., Fukui, Y., Harada, R., et al. 2019, *ApJ*, 886, 15
- van der Tak, F. F. S., van Dishoeck, E. F., Evans, N. J., et al. 2000, *ApJ*, 537, 283
- Whitney, B. A., Sewilo, M., Indebetouw, R., et al. 2008, *AJ*, 136, 18
- Williams, J. P., Blitz, L., & McKee, C. F. 2000, *Protostars and Planets IV*, 97
- Wong, T., Whiteoak, J. B., Ott, J., et al. 2006, *ApJ*, 649, 224
- Wong, T., Hughes, A., Ott, J., et al. 2011, *ApJS*, 197, 16
- Yamaguchi, R., Mizuno, N., Onishi, T., et al. 2001, *PASJ*, 53, 959
- Zinchenko, I., Caselli, P., & Pirogov, L. 2009, *MNRAS*, 395, 2234